

SCIENTIFIC REPORTS

OPEN

Origin of the catalytic activity of phosphorus doped MoS₂ for oxygen reduction reaction (ORR) in alkaline solution: a theoretical study

Cheng Liu, Huilong Dong , Yujin Ji , Tingjun Hou & Youyong Li

Phosphorus doped MoS₂ nanosheets (P-doped MoS₂) have been reported as excellent oxygen reduction reaction (ORR) catalysts with four-electron selectivity in alkaline solution. By performing density functional theory (DFT) calculations, we revealed the detailed reaction mechanism and the key reaction sites on surface of P-doped MoS₂ for ORR catalysis. The double P-doped MoS₂ (2P-MoS₂) is calculated to be more stable than the single P-doped MoS₂ (P-MoS₂), and the configuration with two P atoms in neighboring sites exhibits the highest stability. The surface of P-doped MoS₂ is found highly active for dissociation of O₂. Comparative calculations reveal that P-MoS₂ is unsuitable as ORR catalyst due to the high dissociation barrier of H₂O (1.19 and 2.06 eV for the first and second adsorbed H₂O), while the 2P-MoS₂ shows good ORR catalytic activity with much lower dissociation barrier of H₂O (0.62 eV). Furthermore, we elucidated that the ORR catalytic activity in 2P-MoS₂ originates from the activated S2 atom, which provides an extra adsorption site for the first H₂O and the following OH group benefited from the enhanced hydrogen bond interaction. Our results illustrate the mechanisms of doped MoS₂ based catalysts and provide rational way for designing ORR catalysts with high activity.

Because of the high energy density, high theoretical efficiency, and negligible emission of exhausted gases, fuel cells (FCs) are considered to be one of the most promising energy conversion devices^{1,2}. As the crucial process in FCs, the oxygen reduction reaction (ORR) has been extensively studied^{3–5}. Platinum (Pt) based ORR electro-catalysts are widely used because of their relatively low over-potential in practical applications^{6–8}. However, due to their high cost, less abundance, poor stability in an electrochemical environment, and still sluggish kinetics^{5,9,10}, there are worldwide research efforts to find precious-metal-free catalysts as replacement to Pt based catalysts, such as nonprecious metals, their alloys or oxides, and nitrogen-coordinated metals^{11–13}. As the ideal candidates, metal-free carbon materials doped with heteroatoms (N, B, Si, P, S and F), have been demonstrated to be effective precious-metal-free ORR catalysts^{14–25}.

Since the discovery of the ultrathin MoS₂ monolayer, the electro-catalytic property has attracted great attention^{26–29}. It was reported that with the decrease of monolayer size, MoS₂ reveals favorable performance in ORR and hydrogen evolution reaction (HER)²⁹. By examining nine different layered group 5 metallic transition-metal dichalcogenides (TMDs), Chia *et al.* identified VTe₂ as the best electrocatalyst for the HER in terms of HER over-potential and Tafel slope, at 0.5 V vs. RHE and 55 mV dec⁻¹, respectively³⁰. Also, other TMDs, such as TaS₂, have been found to be efficient catalysts for the ORR due to the onset potentials similar to that of Pt/C catalysts³¹. Luxa *et al.* held the view that the increased activity of 2HTaS₂ may actually stem from the presence of oxides (Ta₂O₅) formed during the oxidation³¹. Another way to improve the electrocatalysis activity is to transform the TMDs from the semiconducting 2H phase to the metallic 1T phase, such as the improved HER performance on the catalyst MoS₂ and WS₂ with p-doping Niobium and Tantalum³². Both experiments and theoreticians suggested that the band gap of TMDs can be tuned by creating their solid solutions either by having metal dichalcogenides with mixed metal elements (i.e., Mo_xW_{1-x}S₂ (0 ≤ x ≤ 1)³³ or mixed chalcogenides (i.e., Mo_ySe_{2-y} (0 ≤ y ≤ 2))³⁴, which make a contribution to electrocatalytic properties toward HER³⁵. In order to improve the performance in electro-catalysis without the using of precious metal, N- and P-doped MoS₂ with few layers were prepared

Institute of Functional Nano & Soft Materials (FUNSOM), Soochow University, Suzhou, Jiangsu, 215123, China. Correspondence and requests for materials should be addressed to H.D. (email: huilong_dong@126.com) or Y.L. (email: yyli@suda.edu.cn)

	Mo-P bond energy (eV)	Relative height of P (Å)	Formation energy (eV/atom)
MoS ₂	–	0	–0.052
P-MoS ₂	4.847 (Mo-P)	–0.023	–0.070
2P-MoS ₂ (1)	4.966 (Mo-P)	–0.109	–0.077
2P-MoS ₂ (2)	4.846 (Mo-P)	–0.089	–0.079
2P-MoS ₂ (3)	4.881 (Mo-P)	–0.093	–0.079

Table 1. The calculated bond energy, the height of P atom and formation energy for pristine, P-MoS₂ and 2P-MoS₂.

experimentally. The experimental data indicate that N- and P-doped single layered MoS₂ possess wonderful ORR catalytic performance in acidic and alkaline environment, respectively^{36,37}. Soon after, the mechanism about the ORR catalytic effect on N- and P-doped MoS₂ single layer is studied by simulations³⁸. However, the catalytic mechanism on the experimental results of P-doped 2D materials as ORR catalysts is not studied, especially the reported generation of extra ORR activity on P-doped MoS₂ nanosheet with four-electron selectivity in alkaline solution, which have been successfully synthesized via the method of pyrolysis³⁷. More importantly, Huang and the co-worker have found through the mapping analysis that, P doping on the MoS₂ monolayer can be dispersed on the surface evenly, and with the increase of P-doping amount, the activity of P-doped MoS₂ on ORR can be improved obviously, which reveals that the active site should be related with the P atoms.

In this work, by density functional theory (DFT) calculations, we explored the origin of catalytic activity in the P-doped MoS₂ monolayer as the ORR electrocatalyst. Previous theoretical and experimental studies³⁷ have indicated that, the P-doped MoS₂ monolayer prefers to work as ORR catalyst in alkaline solution rather than acid solution. According to our simulation results, the P-doped MoS₂ with doping concentration of 5.5% is optimal for ORR catalytic activity (the optimal value observed experimentally is 4.7%³⁷), since it results in stable adsorption of H₂O molecule and the extra OH group through the activated S site, and facilitates the following ORR steps to proceed with a lower barrier in alkaline media. Our work reveals the origin of catalytic activity of P-doped MoS₂ in catalyzing ORR in alkaline solution and provides rational proposal for designing novel ORR catalysts.

Results and Discussion

Characterization of P-doped MoS₂. Before the researches on ORR catalytic performance of P-doped MoS₂ nanosheets, we first characterized their structural stability, structural and electronic properties, and pristine MoS₂ 3 × 3 supercell is taken as comparison. The stability of pristine MoS₂ and P-doped MoS₂ are estimated by computing their formation energies (E_f) as follows,

$$E_f = (n_{Mo}\mu_{Mo} + n_S\mu_S + n_P\mu_P - E_{total})/N, \quad (1)$$

where E_{total} is the total energy of the nanosheet, n_{Mo} , n_S , and n_P are the numbers of Mo, S, and P atoms in the cell. N is the total number of the atoms. μ_{Mo} , μ_S , and μ_P are the chemical potentials of Mo, S, and P, respectively. μ_P is obtained from black phosphorus, while μ_{Mo} is obtained from bulk molybdenum and μ_S is obtained from bulk MoS₂ by subtracting the chemical potential of Mo, respectively. According to the definition, the formation energies of MoS₂, P-MoS₂ and three types of 2P-MoS₂ are calculated as –0.052, –0.070, –0.103, –0.105, and –0.105 eV/atom, respectively (as listed in Table 1). Compared with the pristine MoS₂ and P-MoS₂, 2P-MoS₂ monolayers exhibit very close formation energy (around 0.1 eV/atom), indicating that the P-doping concentration can be increased from 3.7 atom% to 5.5 atom% easily on pristine MoS₂ monolayer.

The bond energy is another parameter to be compared. The bond energy is calculated as followed:

$$E_{bond} = (nE_P + E_D - E_{total})/n, \quad (2)$$

where E_{total} is the total energy of nanosheet, n is the number of P atom, the E_P and E_D denote the energy of isolated P atom and the energy of MoS₂ sheet with vacancy defect (VS), respectively. As listed in Table 1, all the 2P-doped ones have as twice as larger Mo-P bond energy than single P-doped one, indicating the significantly higher stability of Mo-P bond in 2P-MoS₂ than that in P-MoS₂. As a comparison, the bond energy of Mo-S bond in pristine MoS₂ is 0.224 eV, which is only slightly larger than those of Mo-P bond in 2P-MoS₂. Attributing to the neighboring position of P and S in periodic table, the doping of P doesn't affect the initial structure of MoS₂ monolayer much, which can be confirmed by the few relative height of P in doped MoS₂.

By comparing the internal energy of three different 2P-doping MoS₂ monolayers through different softwares (see Table S1), we confirm that the doped P atoms in MoS₂ tend to distribute locally (Fig. 1c) other than separately. Thus the first type of 2P-doping MoS₂ should be the most stable configuration, which is the most possible to be experimentally prepared. This could be further validated by the tendency study. As shown in Fig. S3, we evaluated the tendency of increasing P doping concentration against the energy difference between locally distributed one and separately distributed one. A significant tendency is revealed that with the doping concentration of P increasing, the energy difference between locally distributed one and separately distributed one also increases. Thus it is not accidental that 2P-MoS₂ (1) shows the highest stability among the three configurations, and P in P-doped MoS₂ prefers to distribute locally.

Then the electronic properties of P-doped MoS₂ are evaluated. As displayed in Fig. 1, we plotted the band structures of the P-MoS₂ and 2P-MoS₂, along with the pristine MoS₂ as comparison. Our DFT results indicate that the doping of P leads to vanishing of energy gap [zero gap for P-MoS₂, 2P-MoS₂(2) and 2P-MoS₂(3), and

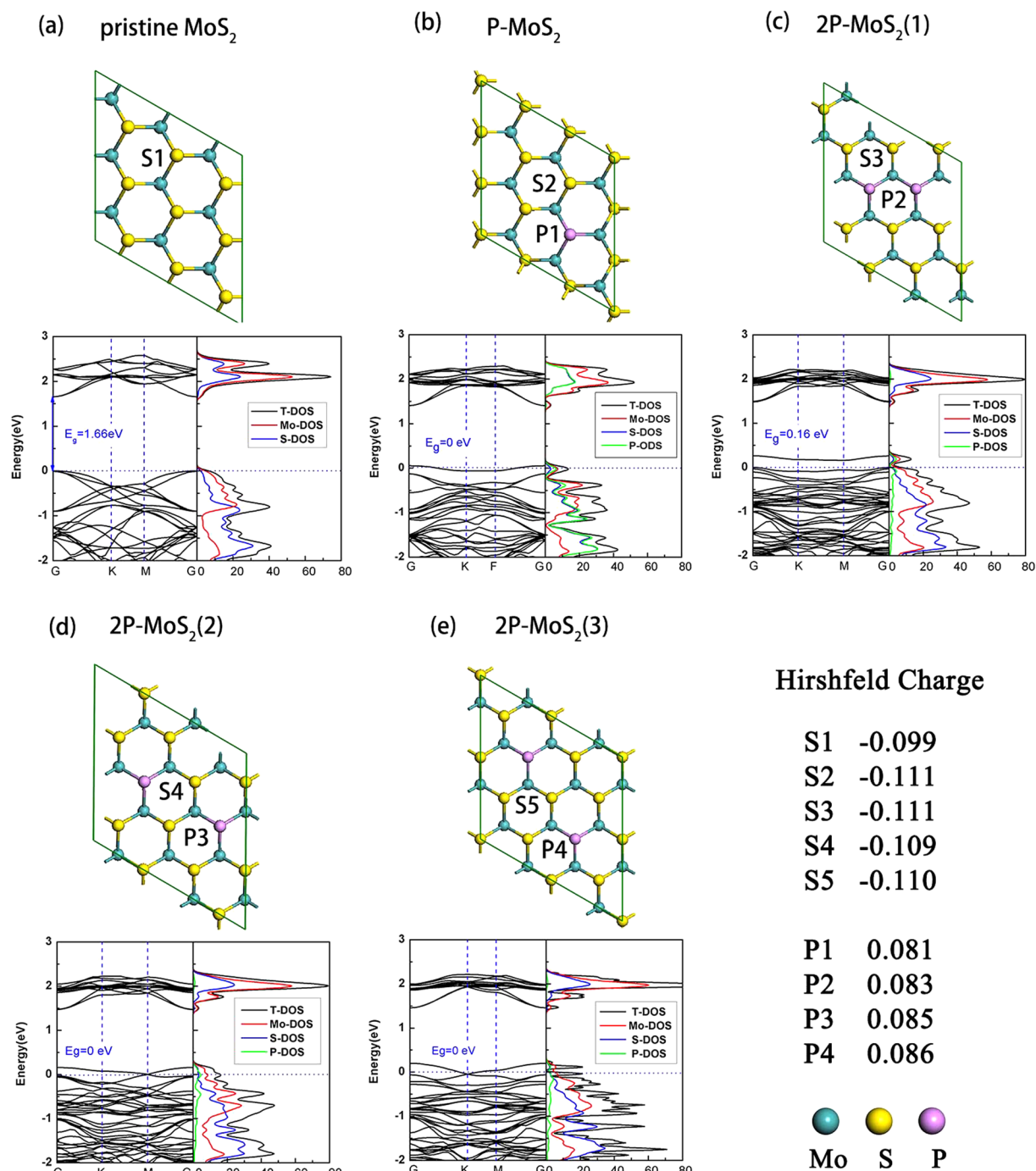


Figure 1. The top view of the optimized structure of (a) pristine MoS₂ nanosheets, (b) single P-doped MoS₂ nanosheets and (c–e) double P-doped MoS₂ nanosheets, respectively. The band structures and corresponding partial density of states (PDOS) are also given. The Hirshfeld charge population of the corresponding atom is also given.

0.16 eV for 2P-MoS₂(1)] compared with the pristine MoS₂ (1.66 eV). This is mostly due to the introduction of impurity band, which exists as a single band across or above the Fermi level that is splitting from valence band edge. Further analysis from partial density of states (PDOS) tells that the splitting of impurity band origins from the orbital hybridization between Mo and P, as shown from PDOS plots in Fig. 1. The small or zero gap induced by doping of P not only greatly enhances the conductivity of MoS₂, but also facilitates the chemical reactivity.

Additionally, the difference of electronegativity between S and P atom also plays important role on the charge population. As shown in Fig. 1, the S atoms (S2–S5) surrounding the doped P atom carry more negative charge (about $-0.11 |e|$) than that in pristine MoS₂ (S1, $-0.099 |e|$). Meanwhile P atoms carry positive charges (more than $+0.08 |e|$), which renders the P atom as suitable adsorption site for the nucleophilic species.

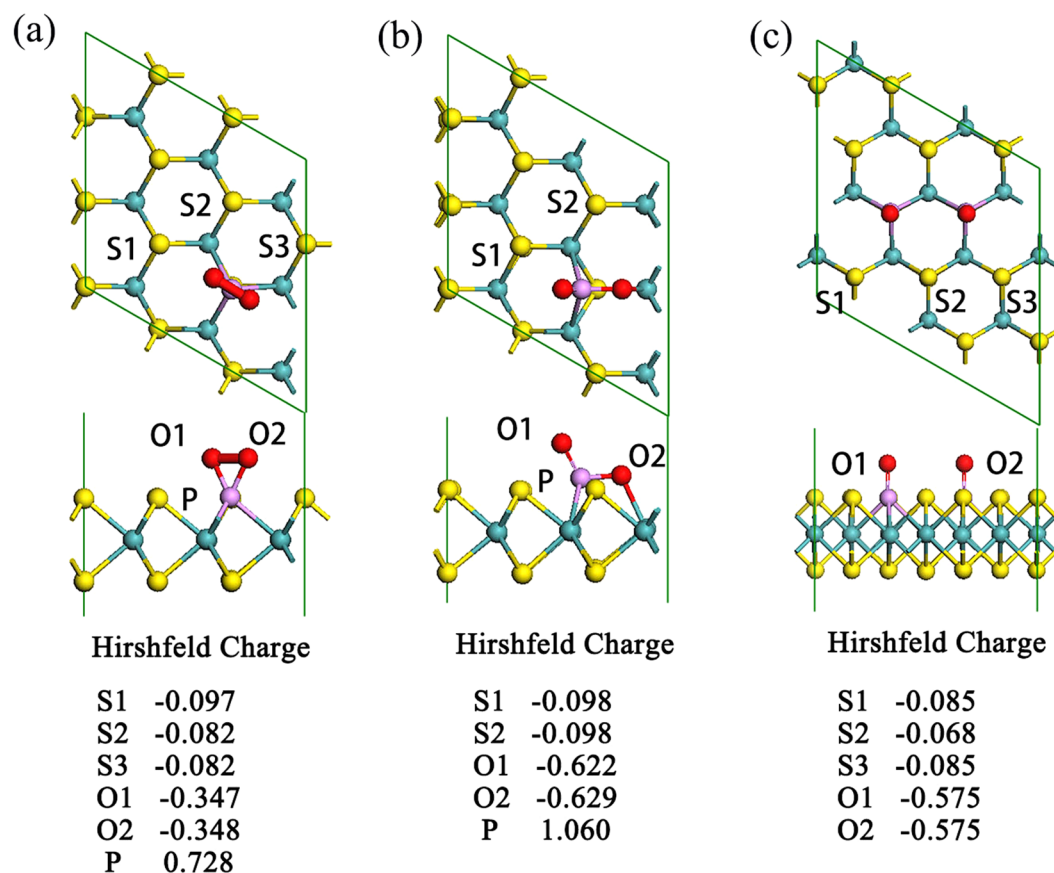


Figure 2. The top and side views of the optimized adsorption configurations of (a) O_2 adsorbed P-MoS₂, (b) 2O adsorbed P-MoS₂ and (c) 2O adsorbed 2P-MoS₂ (1). The Hirshfeld charge values of the corresponding atoms are also given.

The adsorption of O_2 on P-doped MoS₂. As the very beginning of ORR, adsorption of O_2 is taken into consideration first. By putting O_2 molecule on different sites on P-MoS₂ and comparing their E_{ads} , we determined the most energetically favorable adsorption configuration as shown in Fig. 2a. As we can see, the O_2 molecule chemisorbs to the P-MoS₂ by bonding with P atom. The bond length of P-O bonds is about 1.670 Å. And the calculated adsorption energy of O_2 on P-MoS₂ is up to $E_{ads} = -1.11$ eV, which is much more favorable than that on pristine MoS₂ monolayer (-0.11 eV). And the charge transferred from P-MoS₂ to O_2 is as much as $Q = 0.695$ |e| (in ref.³³, $E_{ads} = -0.93$ eV and $Q = 0.30$ |e|). Further results from TS search show that the chemisorbed O_2 can be easily dissociated into two O atoms by overcoming a negligible energy barrier (about 0.05 eV). As shown in Fig. 2b, the two dissociated O atoms adsorb on the top site of P atom and the bridge site between P and Mo atoms, respectively. Similarly, the adsorption of other ORR species (OH and H₂O) also prefers to adsorb onto the P atom, as displayed in Fig. S1 of Supporting Information.

There are two different occasions for adsorption of O_2 molecule on 2P-MoS₂. For 2P-MoS₂ (1), the O_2 molecule binds with the two neighboring P sites with bridged configuration. For 2P-MoS₂ (2) and (3), it is found that due to the large distance between the two P atoms, O_2 molecule can only separately bind with one P atom as the situation of P-MoS₂ (Fig. S1). In the following discussion, we only investigated the adsorption performance of O_2 on 2P-MoS₂ (1), not only due to its highest stability among the 2P-MoS₂, but also for its different binding configuration with O_2 compared with P-MoS₂. Resulting from the high chemical activity of the two adjacent P atoms, the O_2 molecule will directly dissociate and form two P=O bonds without any energy barrier, as shown in Fig. 2c. The bond length of the two P=O bonds are 1.505 Å, which is shorter than the P=O bond (1.515 Å) formed on P-MoS₂.

The charge population of P-MoS₂ and 2P-MoS₂ (1) after dissociation of O_2 is also compared. It is found that comparing with the S atoms (S1 and S2) in P-MoS₂, the S atoms surrounding dopants (S1, S2, and S3 in Fig. 2c) on 2P-MoS₂ carry less negative electron, which may be favorable for the ORR steps as we will discuss in the following parts.

ORR on P-MoS₂. Generally, the total reaction in alkaline solution can be expressed as a 4-electron evolution (*denotes the adsorbed surface):



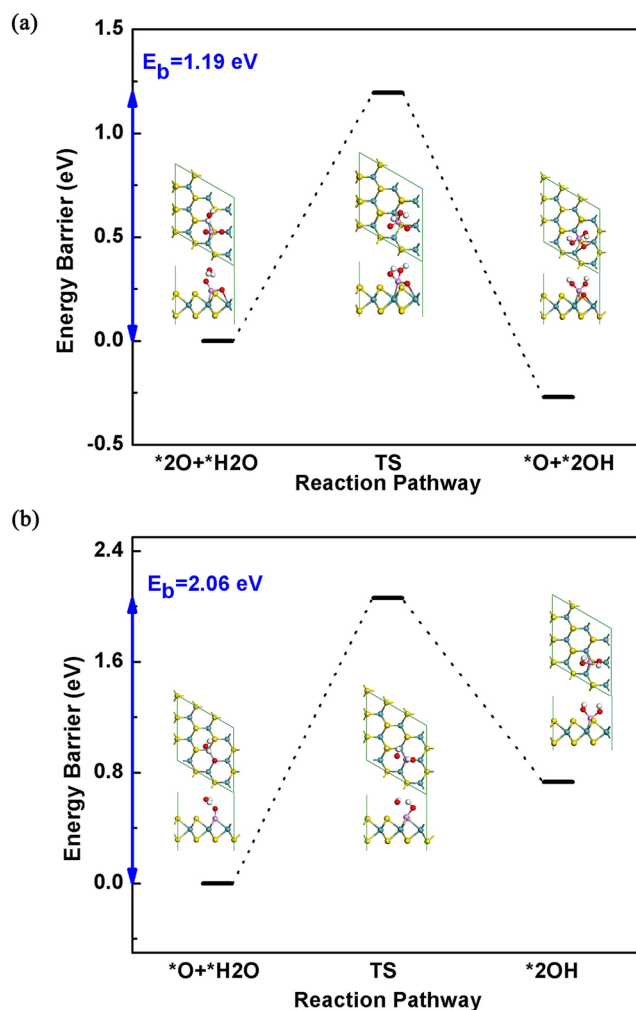


Figure 3. The top and side views of optimized reactant and product as well as the reaction energy barrier for the dissociation of (a) first H₂O and (b) second H₂O. E_b in the diagram represents the barrier energy for each step. The dash line between O atom and H in H₂O represents the effect of hydrogen bonding.

The elementary reaction steps could be expressed as:



After the determination of adsorption and dissociation of O₂, we then proposed the ORR pathway in alkaline environment by taking H₂O molecule into consideration. Due to the lack of adsorption site, our simulation results indicate that the first H₂O can only adsorb on the top of P=O bond by hydrogen bond, as shown in Fig. 3a. One of the H atoms in H₂O will then transfer to the P=O and finally form two adsorbed OH groups as the product. In the most stable configuration of (2OH* + O*), the bridged O atom will move to form two Mo–O bonds with the breaking of Mo–P bond, as a result of steric repulsion from the two OH groups. The activation barrier for this reaction is 1.19 eV, fairly high for room temperature reaction.

Similarly, the dissociation of second H₂O molecule also takes place on the top site of the P=O bond, as shown in Fig. 3b. The activation barrier for this reaction is up to 2.06 eV, even higher than the dissociation of first H₂O. Moreover, this reaction is endothermic with reaction energy of 0.73 eV, which is thermodynamically unstable. The high activation barrier for dissociation of H₂O demonstrates that the catalytic activity of P-MoS₂ is low for ORR, which mainly due to the strong P=O bond and low reaction activity of H₂O on P-MoS₂. This is in consistent with the previous theoretical investigations³⁸.

ORR on 2P-MoS₂. As is presumed from the charge population and electrostatic potential (ESP, shown in Fig. S2) distribution, the two adjacent doping P atoms on the 2P-MoS₂ (1) should be the most active sites for ORR.

	MoS ₂	P-MoS ₂	O-P-MoS ₂	2O-P-MoS ₂	2P-MoS ₂	O-2P-MoS ₂	2O-2P-MoS ₂
E _(ads) /eV	-0.151	-0.129	-0.305	-0.256	-0.120	-0.372	-0.319

Table 2. The adsorption energy of H₂O molecule on the substrates of pristine MoS₂, P-MoS₂, 2P-MoS₂, single O atom adsorbed P-MoS₂ and 2P-MoS₂, as well as two O atoms adsorbed P-MoS₂ and 2P-MoS₂, respectively.

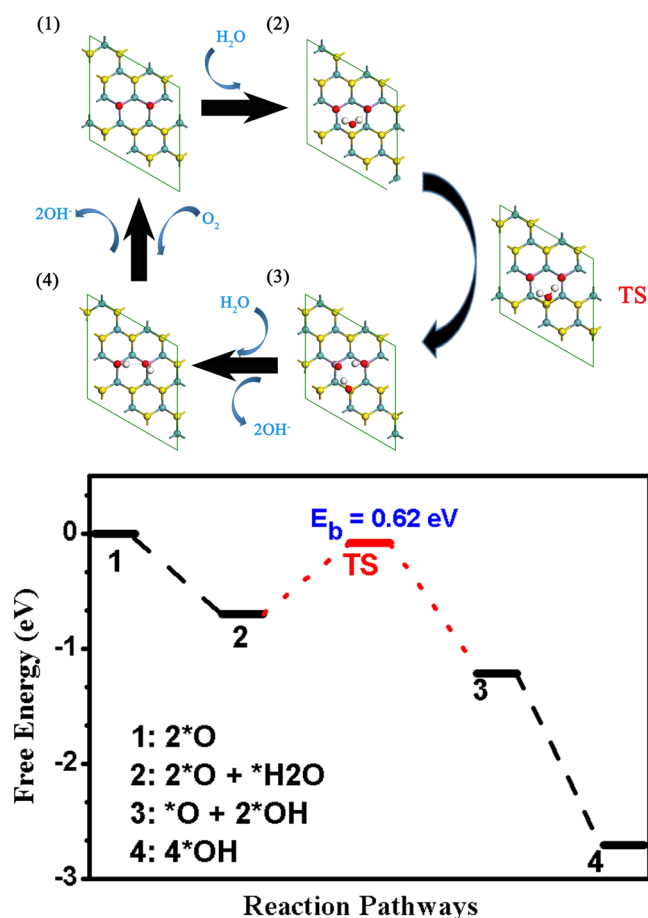


Figure 4. The optimized structure configuration of reactant, intermediates and product (1~4) and the corresponding reaction pathways of ORR on 2P-MoS₂ sheet in alkaline environment.

Same with the P-MoS₂, H₂O molecule physisorbs on 2P-MoS₂, mostly relying on the hydrogen bonds between H atoms in H₂O and P=O bonds, as shown in Fig. 4c. However, the adsorption of H₂O on 2O adsorbed 2P-MoS₂ (1) is obviously strengthened as listed in Table 2. It is found that the decrease of charge assigned on S2 (Fig. 2c) accounts for the improved adsorption performance of H₂O. As we can see in Fig. 2c, due to the strong electronegativity of O, the presence of dissociated O atoms will decrease the negative charge of the surface S atoms. Interestingly, the S2 in 2O adsorbed 2P-MoS₂ (1) exhibits much less negative charge (−0.068 |e| as marked in Fig. 2c) other than that in 2O adsorbed P-MoS₂ (−0.098 |e| as marked in Fig. 2b). It is the charge decrease as well as stronger hydrogen bond caused by the two nearby P=O bonds [as depicted in structure (2) of Fig. 4] together enhance the adsorption performance of H₂O on the S2 site. Combined with the fact that the adsorption of H₂O is strengthened, we assumed that it is this S2 atom that makes 2P-MoS₂ (1) different, and further simulations confirm our proposal. We found that this S2 site can also serve as an adsorption site for OH group, which makes it active during the reaction. As the structure (2) displayed in Fig. 4, accompanied with the hydrogen bond interaction from two P=O bonds, the first added H₂O molecule could be easily dissociated into two adsorbed OH groups, one binds with the P and the other one adsorbs onto the S2 site. The corresponding activation barrier for the dissociation of first H₂O is 0.62 eV, a moderate value for reaction under room temperature. As comparison, both the two dissociated OH groups in P-MoS₂ can only adsorb onto the P atom, leading to significant structural distortion and a high barrier of 1.19 eV.

Following that, the formed OH groups would combine with the electron provided from the electrode and solve into the solution as OH[−]. And then, the exposed P atom will be the most active site on the surface of 2P-MoS₂ (1). Both of the strong reaction activity of P atom and the negative charge on O atom contribute to the dissociation of the second H₂O without energy barrier. Also, the possibility of the breaking of P=O bond and the

formation of OH on P atom is strongly related with the assist of the hydrogen-bond. The whole reaction circulation and the corresponding energy profile of reaction pathway are shown in Fig. 4.

Comparison between P-MoS₂ & 2P-MoS₂. Comparing 2P-MoS₂ with P-MoS₂, the most significant difference is the activation of the S nearby the doping P atoms (as shown in Fig. 2c) and the strong hydrogen-bond existed in 2O-2P-MoS₂, which leads to the enhanced adsorption for H₂O and the chemisorption of OH on S atom during the dissociation of H₂O molecule. Resulting from the more stable adsorption of H₂O as well as the OH group on the activated S site, the reaction energy barrier for the dissociation of the first H₂O is greatly lowered compared with the P-MoS₂ (0.62 eV for 2P-MoS₂ and 1.19 eV for P-MoS₂). Associated with the fact that the formation energy for 2P-MoS₂ is almost the same with the P-MoS₂ (Table 1), it is much easily for 2P-MoS₂ to be prepared experimentally. Meanwhile, among the 2P-MoS₂ nanosheets, type 1 is the most energetically favorable (Table S1). Based on the comparison results, we confirm that the activated S atom in 2P-MoS₂ is the origin of ORR catalytic activity of P-doped MoS₂ in alkaline solution. Notably, it is not accident that the 2P-MoS₂ we modeled shows improved ORR catalytic performance. As we have stated, the doping concentration of 2P-MoS₂ is 5.5%, which is quite close to the optimal doping concentration observed experimentally (4.7%)³⁷. It is the special structure of 2P-MoS₂ that activates the S2 site and facilitates the adsorption of H₂O molecule and the extra OH group, which well explains why the MoS₂ with a P doping concentration of 4.7% exhibits the best ORR performance in experiments.

Conclusions

In summary, we performed comprehensive studies on the origin of the ORR catalytic activity of P-doped MoS₂ in alkaline solution through DFT calculations. The 2P-MoS₂ with doping concentration of 5.5% is calculated to be more stable than the P-MoS₂ with doping concentration of 3.7%, which is consistent with the optimal doping concentration of 4.7% from the experiments³⁷. And the configuration with two P atoms in neighboring sites is found to possess the highest stability among the possible configurations of 2P-MoS₂. The surface of P-doped MoS₂ exhibits highly reactive activation for dissociation of O₂.

Except the doping on MoS₂ plane, we also discuss the influence of phosphorus present on edge of MoS₂. The detailed structure configuration and energy values have been given in Fig. S6. For the two edge S sites that can be placed by P (Mo edge and S edge as shown in Fig. S6 (a)), the P prefer doping in S edge site rather than Mo edge site considering the relative energy difference up to 0.97 eV. For the O₂ adsorption on the P-doped MoS₂ on the edge site, two adsorption sites are considered (shown in Fig. S6 (b)). The positive adsorption energy on the S site indicated that P-doped on the edge site can't activate the S site around P atom. While on the edge P site, the adsorbed O₂ would dissociated directly, which is same with single P atom doped on MoS₂ plane (Fig. 2 (b)). And the adsorption for H₂O is -0.13 eV, which is also the same with the P-MoS₂ (-0.129 eV, as shown in Table 2). Thus, based on our calculation results, we concluded that the doping of P in the basal plane and edge sites will exhibit similar adsorption performance for adsorption of H₂O and dissociation for O₂.

Further comparative calculations reveal that P-MoS₂ is unsuitable as ORR catalyst due to the strong P=O bond and high dissociation barrier of H₂O on P-MoS₂ (1.19 eV and 2.06 eV for the first and second adsorbed H₂O). In comparison, the 2P-MoS₂ shows good ORR catalytic activity. The dissociation barrier of the first H₂O on 2P-MoS₂ (0.62 eV) is much lower than that of P-MoS₂. And the dissociation of O₂ and the second H₂O on 2P-MoS₂ is even spontaneous without any activation barriers. While for the two other types of 2P-doped MoS₂, not only the stability is less than the neighboring doped 2P-MoS₂, but also the reaction mechanism is similar with the single P doped MoS₂. By checking the charge population and adsorption performance of the ORR intermediates, we elucidated that the ORR catalytic activity in 2P-MoS₂ originates from the activated S2 atom with increased charge that affected by the two neighboring P=O bonds, which provides an extra adsorption site for the first H₂O and the following OH group with the help from the enhanced hydrogen bond interaction. Our results reveal the detailed reaction mechanism of MoS₂ based catalysts and provides instructive suggestions for designing ORR catalysts with high performance.

Methods

All the calculations are carried out by DMol³ program. The electronic exchange and correlation effects are described by the generalized gradient approximation with Perdew–Burke–Ernzerhof (GGA-PBE) functional³⁹. In order to accurately describe the van der Waals forces, dispersion correction (DFT-D) is adopted by Grimme approach⁴⁰. The all-electron double numerical atomic orbital including polarized p-function (DNP)⁴¹ is chosen as the basis set with orbital cutoff of 4.9 Å. The convergence threshold values for energies, gradient and displacement are specified as 1×10^{-5} Ha, 1×10^{-3} Ha/Å, and 5×10^{-3} Å, respectively, while the self-consistent-field (SCF) convergence threshold value is 1×10^{-6} Ha. To enhance SCF convergence efficiency during optimization, an electron thermal smearing value of 0.002 Ha is employed for all the calculations. The conductor-like screening model (COSMO)⁴² is used to simulate the aqueous environment, where the dielectric constant is set as 78.54 (water). All the stably existed species during the ORR process are confirmed no imaginary frequencies by performing frequency analysis. To determine the activation barriers (E_a), transition state (TS) searches are conducted by using the complete linear synchronous transit/quadratic synchronous transit (LST/QST) method. All the obtained TS structures exhibit only one imaginary frequency throughout the potential surface, and are ensured to directly connect corresponding reactants and products by nudgedelastic band (NEB) algorithm⁴³.

The unit cell of 2H-MoS₂ is optimized by using $9 \times 9 \times 1$ Monkhorst-Pack k-point grids. The single P doped MoS₂ is then obtained by substituting a surface S atom in MoS₂ 3×3 supercell into P atom, with a doping concentration of 3.7 atom%. The structures of MoS₂ 3×3 supercell and single P-doped MoS₂ nanosheet (P-MoS₂) are depicted in Fig. 1(a,b). The double P-doped MoS₂ nanosheet (2P-MoS₂) is obtained by substituting two surface

S atoms in MoS₂ 2√3 × 2√3 supercell into P atoms, with a doping concentration of 5.5 atom%. Differing from the relative positions between the two doped P atoms, there are three possible configurations that are taken into consideration. That is, neighboring sites (type 1), spaced by a Mo atom (type 2), and spaced by a S atom (type 3), as shown in Fig. 1(c–e). Considering the close atomic volume between P and S atom, the influence of doping on lattice size is neglected. Brillouin zone of MoS₂ 3 × 3 supercell and the P-doped MoS₂ structures are sampled by 3 × 3 × 1 Monkhorst-Pack k-point grids during the geometry optimization, which is tested converging for total energy. Population analysis of electron is performed by assigning Hirshfeld charges⁴⁴ for the optimized structures.

In this article, the adsorption energy (E_{ads}) is defined as

$$E_{ads} = E_{mol/sub} - E_{mol} - E_{sub} \quad (7)$$

Where E_{mol} and E_{sub} represent the total energies of the isolated adsorbate and adsorption substrate, and $E_{mol/sub}$ represents the total energy of the adsorption system. Here, the negative E_{ads} means exothermic process for adsorption. The more negative E_{ads} is, the more stable the adsorption system is. The triplet is taken as the ground state of O₂ during the calculation.

In order to calculate the Gibbs free energy of reactions involving electron/proton transfer, the computational hydrogen electrode (CHE) model introduced by Nørskov and co-workers was used⁴⁵. The reaction free energies (ΔG) can be computed as follows:

$$\Delta G = \Delta E + \Delta ZPE - T\Delta S + \Delta G_{pH} + \Delta G_U \quad (8)$$

where the ΔE was the reaction total energy directly obtained from Dmol3 calculation, ΔZPE is the change in the zero-point energy, T is the temperature (298.15 K), and ΔS is the change in entropy. $\Delta G_{pH} = K_b T \times \ln 10 \times \text{pH}$ represents the free energy contribution due to the variation in the H concentration, and the pH value in this work was assume to 14 in the alkaline medium. $\Delta G_U = -neU$, where n was the number of electrons transferred and U was the applied electrode potential. The entropy values are taken from the physical chemistry table considering H₂ and H₂O in gaseous form at room temperature and atmospheric pressure whereas the entropy of the adsorbed state is considered to be negligible. ZPE of the free molecules are estimated from our DFT calculations considering vibrational frequencies of the molecules in the harmonic approximation. The details of calculation steps to plot Free energy profile are demonstrated in the supporting information.

References

1. Debe, M. K. Electrocatalyst approaches and challenges for automotive fuel cells. *Nature* **486**, 43–51 (2012).
2. Steele, B. C. & Heinzel, A. Materials for fuel-cell technologies. *Nature* **414**, 345–352 (2001).
3. Zhou, M., Wang, H.-L. & Guo, S. Towards high-efficiency nanoelectrocatalysts for oxygen reduction through engineering advanced carbon nanomaterials. *Chem. Soc. Rev.* **45**, 1273–1307 (2016).
4. Armand, M. & Tarascon, J.-M. Building better batteries. *Nature* **451**, 652–657 (2008).
5. Cheng, F. & Chen, J. Metal–air batteries: from oxygen reduction electrochemistry to cathode catalysts. *Chem. Soc. Rev.* **41**, 2172–2192 (2012).
6. Shao, M., Chang, Q., Dodelet, J.-P. & Chenitz, R. Recent Advances in Electrocatalysts for Oxygen Reduction Reaction. *Chem. Rev.* **116**, 3594–3657, <https://doi.org/10.1021/acs.chemrev.5b00462> (2016).
7. Nie, Y., Li, L. & Wei, Z. Recent advancements in Pt and Pt-free catalysts for oxygen reduction reaction. *Chem. Soc. Rev.* **44**, 2168–2201 (2015).
8. Colón-Mercado, H. R. & Popov, B. N. Stability of platinum based alloy cathode catalysts in PEM fuel cells. *J. Power Sources* **155**, 253–263 (2006).
9. Greeley, J. *et al.* Alloys of platinum and early transition metals as oxygen reduction electrocatalysts. *Nat. Chem.* **1**, 552–556 (2009).
10. Morozan, A., Jousselme, B. & Palacin, S. Low-platinum and platinum-free catalysts for the oxygen reduction reaction at fuel cell cathodes. *Energ. Environ. Sci.* **4**, 1238–1254 (2011).
11. Bezerra, C. W. *et al.* A review of Fe–N/C and Co–N/C catalysts for the oxygen reduction reaction. *Electrochim. Acta* **53**, 4937–4951 (2008).
12. Gong, K., Du, F., Xia, Z., Durstock, M. & Dai, L. Nitrogen-doped carbon nanotube arrays with high electrocatalytic activity for oxygen reduction. *Science* **323**, 760–764 (2009).
13. Liu, R., Wu, D., Feng, X. & Müllen, K. Nitrogen-doped ordered mesoporous graphitic arrays with high electrocatalytic activity for oxygen reduction. *Angew. Chem.* **122**, 2619–2623 (2010).
14. Zhang, X. *et al.* The mechanisms of oxygen reduction reaction on phosphorus doped graphene: A first-principles study. *J. Power Sources* **276**, 222–229 (2015).
15. Dong, H. *et al.* Theoretical investigations on SiC 2 siligraphene as promising metal-free catalyst for oxygen reduction reaction. *J. Power Sources* **299**, 371–379 (2015).
16. Wang, L. *et al.* Potential application of novel boron-doped graphene nanoribbon as oxygen reduction reaction catalyst. *J. Phys. Chem. C* **120**, 17427–17434 (2016).
17. Zhang, L. & Xia, Z. Mechanisms of Oxygen Reduction Reaction on Nitrogen-Doped Graphene for Fuel Cells. *J. Phys. Chem. C* **115**, 11170–11176, <https://doi.org/10.1021/jp201991j> (2011).
18. Ding, W. *et al.* Space-Confinement-Induced Synthesis of Pyridinic-and Pyrrolic-Nitrogen-Doped Graphene for the Catalysis of Oxygen Reduction. *Angew. Chem.* **125**, 11971–11975 (2013).
19. Fazio, G., Ferrighi, L. & Di Valentin, C. Boron-doped graphene as active electrocatalyst for oxygen reduction reaction at a fuel-cell cathode. *J. Catal.* **318**, 203–210 (2014).
20. Sheng, Z.-H., Gao, H.-L., Bao, W.-J., Wang, F.-B. & Xia, X.-H. Synthesis of boron doped graphene for oxygen reduction reaction in fuel cells. *J. Mater. Chem.* **22**, 390–395 (2012).
21. Wang, X. *et al.* One-pot synthesis of nitrogen and sulfur co-doped graphene as efficient metal-free electrocatalysts for the oxygen reduction reaction. *Chem. Commun.* **50**, 4839–4842 (2014).
22. Anderson, R. M. *et al.* A theoretical and experimental approach for correlating nanoparticle structure and electrocatalytic activity. *Accounts of chemical research* **48**, 1351–1357, <https://doi.org/10.1021/acs.accounts.5b00125> (2015).
23. Liu, Z. W. *et al.* Phosphorus-doped graphite layers with high electrocatalytic activity for the O₂ reduction in an alkaline medium. *Angew. Chem.* **123**, 3315–3319 (2011).
24. Gusmao, R., Sofer, Z., Sembera, F., Janousek, Z. & Pumera, M. Electrochemical Fluorographane: Hybrid Electrocatalysis of Biomarkers, Hydrogen Evolution, and Oxygen Reduction. *Chemistry* **21**, 16474–16478, <https://doi.org/10.1002/chem.201502535> (2015).

25. Wong, C. H., Sofer, Z., Klimova, K. & Pumera, M. Microwave Exfoliation of Graphite Oxides in H₂S Plasma for the Synthesis of Sulfur-Doped Graphenes as Oxygen Reduction Catalysts. *ACS applied materials & interfaces* **8**, 31849–31855, <https://doi.org/10.1021/acsami.6b10199> (2016).
26. Li, Y. *et al.* MoS₂ nanoparticles grown on graphene: an advanced catalyst for the hydrogen evolution reaction. *JACS* **133**, 7296–7299 (2011).
27. Liu, K.-K. *et al.* Growth of large-area and highly crystalline MoS₂ thin layers on insulating substrates. *Nano Lett.* **12**, 1538–1544 (2012).
28. Wu, S. *et al.* Electrochemically reduced single-layer MoS₂ nanosheets: Characterization, properties, and sensing applications. *Small* **8**, 2264–2270 (2012).
29. Wang, T. *et al.* Size-Dependent Enhancement of Electrocatalytic Oxygen-Reduction and Hydrogen-Evolution Performance of MoS₂ Particles. *Chemistry* **19**, 11939–11948, <https://doi.org/10.1002/chem.201301406> (2013).
30. Xinyi Chia, A. A., Lazar, P. & Sofer, Z. and Martin Pumera. Electrocatalysis of layered Group 5 metallic transition metal dichalcogenides (MX₂, M = V, Nb, and Ta; X = S, Se, and Te). *J. Mater. Chem. A*. <https://doi.org/10.1039/C6TA05110C> (2016).
31. Luxa, J. *et al.* 2H-→1T Phase Engineering of Layered Tantalum Disulfides in Electrocatalysis: Oxygen Reduction Reaction. *Chemistry* **23**, 8082–8091, <https://doi.org/10.1002/chem.201701494> (2017).
32. Chua, X. J. *et al.* Negative Electrocatalytic Effects of p-Doping Niobium and Tantalum on MoS₂ and WS₂ for the Hydrogen Evolution Reaction and Oxygen Reduction Reaction. *ACS Catal.* **6**, 5724–5734, <https://doi.org/10.1021/acscatal.6b01593> (2016).
33. Lin, Z. *et al.* Facile synthesis of MoS₂ and Mo_xW_{1-x}S₂ triangular monolayers. *APL Mater.* **2**, 092514, <https://doi.org/10.1063/1.4895469> (2014).
34. Kutana, A., Penev, E. S. & Yakobson, B. I. Engineering electronic properties of layered transition-metal dichalcogenide compounds through alloying. *Nanoscale* **6**, 5820–5825, <https://doi.org/10.1039/c4nr00177j> (2014).
35. Wang, L., Sofer, Z., Luxa, J. & Pumera, M. Mo_xW_{1-x}S₂ Solid Solutions as 3D Electrodes for Hydrogen Evolution Reaction. *Adv Materials Interfaces* **2**, 1500041, <https://doi.org/10.1002/admi.201500041> (2015).
36. Hao, L. *et al.* Nitrogen-doped MoS₂/carbon as highly oxygen-permeable and stable catalysts for oxygen reduction reaction in microbial fuel cells. *J. Power Sources* **339**, 68–79 (2017).
37. Huang, H., Feng, X., Du, C. & Song, W. High-quality phosphorus-doped MoS₂ ultrathin nanosheets with amenable ORR catalytic activity. *Chem. Commun.* **51**, 7903–7906 (2015).
38. Zhang, H., Tian, Y., Zhao, J., Cai, Q. & Chen, Z. Small Dopants Make Big Differences: Enhanced Electrocatalytic Performance of MoS₂ Monolayer for Oxygen Reduction Reaction (ORR) by N- and P-Doping. *Electrochim. Acta* **225**, 543–550 (2017).
39. Perdew, J. P., Burke, K. & Ernzerhof, M. Generalized gradient approximation made simple. *Phys. Rev. Lett.* **77**, 3865 (1996).
40. Grimme, S. Semiempirical GGA-type density functional constructed with a long-range dispersion correction. *J. Comput. Chem.* **27**, 1787–1799 (2006).
41. Delley, B. An all-electron numerical method for solving the local density functional for polyatomic molecules. *J. Chem. Phys.* **92**, 508–517 (1990).
42. Klamt, A. & Schüürmann, G. COSMO: a new approach to dielectric screening in solvents with explicit expressions for the screening energy and its gradient. *J. Chem. Soc., Perkin Trans. 2*, 799–805 (1993).
43. Henkelman, G. & Jónsson, H. Improved tangent estimate in the nudged elastic band method for finding minimum energy paths and saddle points. *J. Chem. Phys.* **113**, 9978–9985 (2000).
44. Hirshfeld, F. L. Bonded-atom fragments for describing molecular charge densities. *Theor. Chem. Acc.* **44**, 129–138 (1977).
45. Nørskov, J. K. *et al.* Origin of the Overpotential for Oxygen Reduction at a Fuel-Cell Cathode. *The Journal of Physical Chemistry B* **108**, 17886–17892, <https://doi.org/10.1021/jp047349j> (2004).

Acknowledgements

This work is supported by the Ministry of Science and Technology of China (Grants No. 2017YFA0204802 and 2017YFB0701601), the National Natural Science Foundation of China (Grants No. 51761145013, 21673149 and 21703145), China Postdoctoral Science Foundation (Grant No. 2017M611892), and a Project Funded by the Priority Academic Program Development of Jiangsu Higher Education Institutions (PAPD). This is also a project supported by the Fund for Innovative Research Teams of Jiangsu Higher Education Institutions, Jiangsu Key Laboratory for Carbon Based Functional Materials and Devices, Collaborative Innovation Center of Suzhou Nano Science and Technology.

Author Contributions

H.D. and Y.L. conceived the main idea. C.L. performed all the calculation work. C.L. and H.D. analyzed the results and wrote the paper. Y.J. and T.H. joined the discussion. All authors contributed to the final version. Y.L. supervised the project.

Additional Information

Supplementary information accompanies this paper at <https://doi.org/10.1038/s41598-018-31354-0>.

Competing Interests: The authors declare no competing interests.

Publisher's note: Springer Nature remains neutral with regard to jurisdictional claims in published maps and institutional affiliations.



Open Access This article is licensed under a Creative Commons Attribution 4.0 International License, which permits use, sharing, adaptation, distribution and reproduction in any medium or format, as long as you give appropriate credit to the original author(s) and the source, provide a link to the Creative Commons license, and indicate if changes were made. The images or other third party material in this article are included in the article's Creative Commons license, unless indicated otherwise in a credit line to the material. If material is not included in the article's Creative Commons license and your intended use is not permitted by statutory regulation or exceeds the permitted use, you will need to obtain permission directly from the copyright holder. To view a copy of this license, visit <http://creativecommons.org/licenses/by/4.0/>.

© The Author(s) 2018